

Efficiency of Mixing Forced by Unsteady Shear Flow

RYUICHIRO INOUE

Department of Physics and Astronomy, University of Victoria, Victoria, British Columbia, Canada

WILLIAM D. SMYTH

College of Oceanic and Atmospheric Science, Oregon State University, Corvallis, Oregon

(Manuscript received 2 October 2007, in final form 18 December 2008)

ABSTRACT

The dependence of mixing efficiency on time-varying forcing is studied by direct numerical simulation (DNS) of Kelvin–Helmholtz (KH) instability. Time-dependent forcing fields are designed to reproduce a wavelike oscillation by solving the equations of motion in a tilted coordinate frame and allowing the tilt angle to vary in time. Mixing efficiency Γ_c is defined as the ratio of potential energy gain to dissipation, both averaged over one forcing cycle and first examined via parameters characterizing waves: the minimum Richardson number Ri_{\min} and the normalized frequency of the forcing ω/N . The effect of Reynolds number Re_0 and the initial random disturbance amplitude b are also examined. In the experiments presented, Γ_c varies between 0.21 and 0.36 and is controlled by the timing of two events: the emergence of KH billows and the arrival of the deceleration of the mean shear by the wavelike forcing. Here, Γ_c is higher than a canonical value of 0.2 when the deceleration phase of the forcing suppresses the less efficient turbulence after breakdown of KH billows. However, when Ri_{\min} and ω/N are small, KH billows start to develop before Ri_{\min} is achieved. Therefore, the forcing accelerates the mean shear and thereby sustains turbulence after the breakdown of KH billows. The canonical value is then reproduced in the DNS. Although larger values of Re_0 and b intensify the development of KH billows and modify Γ_c , this effect is less significant when forcing fields act to sustain turbulence. The time-averaged Thorpe scale and Ozmidov scale are also used to see how mixing is modified by forcing fields and compared with past microstructure measurements. It is found that DNS also corresponds to past observations if the forcing accelerates the mean shear to sustain turbulence.

1. Introduction

Internal waves are the main cause of turbulence in the thermocline and the deep ocean (Munk 1981; Gregg 1987; Garrett and St. Laurent 2002). Wave–wave interaction theory and microstructure measurements have shown that the turbulent kinetic energy dissipation rate can be estimated from the 10-m vertical shear (e.g., Gregg 1989; Polzin et al. 1995; Sun and Kunze 1999). However, the mixing rate depends further on the mixing efficiency Γ or the buoyancy flux as a fraction of the energy dissipation rate (e.g., Osborn 1980). Osborn (1980) determined Γ to be 0.2 assuming that the steady-state balance is achieved in the ocean mixing caused by

shear instability and that the flux Richardson number (Ri_f) is restricted to a critical value to maintain steady-state turbulence. Here, Ri_f is defined as the ratio of the potential energy gain to the kinetic energy loss and is related to Γ by $\Gamma = Ri_f/(1 - Ri_f)$ in steady-state turbulence. The value 0.2 is often used in the ocean modeling as well as in interpretations of microstructure measurements (Munk and Wunsch 1998; Wunsch and Ferrari 2004; Simmons et al. 2004; Polzin et al. 1997; Arneborg 2002), but it is likely to depend on various factors, such as the duration and intensity of high-shear events, which lead to instability and turbulence (Garrett 2001).

Because of its importance, mixing efficiency for shear-driven turbulence has been studied through in situ ocean observations, laboratory experiments, theories, and numerical simulations. In the ocean observations, Oakey (1982, 1985) defined Γ in stratified steady turbulence that can be estimated from microscale temperature gradient and velocity shear measurements.

Corresponding author address: Ryuichiro Inoue, Ocean Physics Department, Applied Physics Laboratory, University of Washington, 1013 NE 40th St., Seattle, WA 98105-6698.
E-mail: rinoue@apl.washington.edu

Ivey and Imberger (1991) related Γ to two dimensionless parameters (overturn Froude number, the ratio of the largest eddy length without buoyancy effect to the most energetic overturn scale, and overturn Reynolds number, the ratio of the most energetic overturn scale to the smallest length scale in turbulence) from laboratory experiments. Imberger and Ivey (1991) classified observed turbulent events in this parameter space and inferred Γ by different generation processes of turbulence. Moum (1996), Ruddick et al. (1997), and St. Laurent and Schmitt (1999) also followed the definition by Oakey (1982, 1985) and obtained similar values of $\Gamma \approx 0.2 \pm 0.1$ in turbulent patches. Seim and Gregg (1994) observed the evolution and decay of Kelvin–Helmholtz (KH) instability in a tidal channel and found highly variable Γ (0.17–1.3) in each stage of instability and a higher average value of $\Gamma = 0.58$. Gargett and Moum (1995) and Seim and Gregg (1995) pointed out the difference in the definition of Γ in Seim and Gregg (1994), and Γ should be halved for comparison with past studies. Gargett and Moum (1995) also reported Γ is around 0.2 in a tidal front.

Laboratory experiments mainly investigate the ratio of the potential energy gain to the kinetic energy loss Ri_f in turbulent patches. Thorpe (1968) reproduced KH instability in tilted tube experiments, and Thorpe (1973) estimated Ri_f over one tilting experiment and obtained $0.21 < Ri_f < 0.27$ ($0.27 < \Gamma < 0.36$). By using the results from Thorpe (1973) and Koop (1976), Linden (1979) showed that Ri_f over one tilting experiment is a decreasing function of the Richardson number. In theoretical studies, Thompson (1980), inspired by the results of Thorpe (1973), showed that the maximum value of Ri_f in turbulence is equivalent to the critical Richardson number [$Ri_c = 0.25$; Miles (1961); Howard (1961)] from energy budgets. However, he also assumed that vertical eddy diffusivity is the same for momentum and density, that turbulence occurs in a limited region, and that turbulence always exists and has the same intensity when $Ri < Ri_c$. Winters et al. (1995) and Winters and D’Asaro (1996) further explored the energy balance in stratified turbulent events and obtained energy budgets under the Boussinesq approximation. Because this framework is easy to reproduce in a direct numerical simulation (DNS), it becomes the basis for studies using the computational approach.

Due to recent advances in computer resources, DNS has been used to study stratified turbulence. Smyth (1999), Smyth and Moum (2000), Caulfield and Peltier (2000), Staquet (2000), Smyth et al. (2001), and Peltier and Caulfield (2003) reproduced KH instability in unforced shear flow and reported the time-dependent behavior of efficiencies (their definitions of efficiencies are reviewed in Smyth et al. 2007). Caulfield and Peltier

(2000) and Peltier and Caulfield (2003) introduced cumulative mixing efficiency and parameterized cumulative values during the turbulent stage as a function of Richardson number. Staquet (2000) and Smyth et al. (2001) also investigated the complex behavior of instantaneous ratios. Smyth et al. (2001) defined mixing efficiency averaged over one mixing event including a preturbulent stage, and examined dependences on the Richardson and Reynolds numbers. Smyth et al. (2007) and Carpenter et al. (2007) studied mixing efficiency in Holmboe waves. Smyth et al. (2007) suggested that net mixing efficiency is governed by the relative duration and intensity of the preturbulent and turbulent phases.

These numerical studies used unforced shear as a background flow; however, turbulence induced by internal waves may be sensitive to the time evolution of the forcing fields. KH instability associated with internal wave breaking was observed directly by Woods (1968). Internal wave breaking has been studied numerically (Lelong and Dunkerton 1998a,b; Bouruet-Aubertot and Thorpe 1999; Bouruet-Aubertot et al. 2001; Fringer and Street 2003), but there are still limitations of computer resources for reproducing and quantifying turbulence due to wave breaking in large parameter ranges.

The objective of this study is to increase our understanding of mixing efficiency in the ocean by using DNS of KH billows in a time-dependent mean flow with a view toward gaining insight into internal wave breaking. We focus on the relation between mixing efficiency and time-dependent forcing fields. We reproduce time-dependent forcing by solving the equations of motion within a tilted coordinate framework and allowing the tilt angle to vary sinusoidally in time. Spatial and temporal scales are based on the interfacial wave observations of Woods (1968), who shows that interfacial gravity waves break via shear instability in observations of the Mediterranean thermocline.

Dimensional parameters that govern the flow include the maximum buoyancy frequency N , forcing frequency ω , maximum shear $\partial U/\partial z$, molecular viscosity ν , molecular diffusivity κ , and layer half-thickness h . According to Buckingham’s Π theorem (Kundu and Cohen 2008), we can make four independent dimensionless parameters from these six dimensional numbers: the Prandtl number $Pr = \nu/\kappa$, normalized forcing frequency ω/N , Richardson number $Ri = N^2/(\partial U/\partial z)^2$, and Reynolds number $Re = (h^2/\nu)(\partial U/\partial z)$. Since we explore turbulent mixing generated by KH instability over one wavelike forcing cycle, first we evaluate the mixing efficiency as a function of two dimensionless parameters that represent forcing wave properties: the minimum Richardson number achieved in one forcing cycle, Ri_{\min} , and the frequency of tilting compared with the buoyancy

frequency, ω/N . These choices allow us to investigate the behavior of mixing efficiency in energetic and persistent mixing events inferred from the ocean internal wave spectrum (Garrett 2001).

In section 2, we explain our mathematical model and numerical solution methods. Our wavelike forcing field is also explained in detail. Section 3 reviews the basic concepts for quantifying a mixing event. Section 4 describes the main results. We begin by examining the main effect of the wavelike forcing, namely, the deceleration of the mean shear after instability growth has begun. We then look at mixing statistics in various parameter ranges, including high-frequency forcing following those observed by Woods (1968) and lower-frequency forcing that we expect to occur more commonly in the ocean. Dependences on the Reynolds number and on the amplitude of the initial perturbation are also explored. In section 5, we compare DNS results with microstructure measurements via the turbulent kinetic energy equation.

2. Computation method

a. Model equations in the tilted frame

The DNS model used in this study numerically integrates the incompressible equations of motion under the Boussinesq approximation. To represent time-dependent forcing, we write the equations in a coordinate system tilted at an angle $\tau(t)$ from the horizontal:

$$\begin{aligned} \frac{Du}{Dt} &= -\frac{1}{\rho_0} \frac{\partial p}{\partial x} + \nu \nabla^2 u - g \frac{\rho}{\rho_0} \sin \tau + 2 \frac{d\tau}{dt} w, \\ \frac{Dv}{Dt} &= -\frac{1}{\rho_0} \frac{\partial p}{\partial y} + \nu \nabla^2 v, \\ \frac{Dw}{Dt} &= -\frac{1}{\rho_0} \frac{\partial p}{\partial z} + \nu \nabla^2 w - g \frac{\rho}{\rho_0} \cos \tau - 2 \frac{d\tau}{dt} u, \end{aligned} \quad (1)$$

where $D/Dt = \partial/\partial t + \mathbf{u} \cdot \nabla$ and the velocity vector is defined as $\mathbf{u} = (u, v, w)$. The x and y axes are taken to be the streamwise and spanwise directions, respectively, while z is positive upward. The constant ρ_0 is the reference density, p is the pressure, ν is the molecular viscosity, and g is the gravitational acceleration. The tilt angle τ is a function of time and will be discussed in detail below. The final terms in the u and w components of (1) are Coriolis accelerations arising from this time-dependent rotation. Coriolis accelerations due to planetary rotations are not considered. The incompressibility condition is expressed as

$$\nabla \cdot \mathbf{u} = 0. \quad (2)$$

An advection–diffusion equation is used to calculate the density ρ :

$$\frac{D\rho}{Dt} = \frac{\nu}{\text{Pr}} \nabla^2 \rho, \quad (3)$$

where $\nu = 10^{-6} \text{ m}^2 \text{ s}^{-1}$ and $\text{Pr} = 7$. We use only one component for density rather than temperature and salt; therefore, the possibilities of double-diffusive processes and differential diffusion are excluded (e.g., Ruddick et al. 1997). We impose a periodic condition for horizontal boundaries. No-flux and free-slip conditions are imposed at $z = \pm L_z/2$:

$$w \Big|_{z=\pm \frac{1}{2}L_z} = \frac{\partial \rho}{\partial z} \Big|_{z=\pm \frac{1}{2}L_z} = 0, \quad \frac{\partial u}{\partial z} \Big|_{z=\pm \frac{1}{2}L_z} = \frac{\partial v}{\partial z} \Big|_{z=\pm \frac{1}{2}L_z} = 0. \quad (4)$$

Here, L_x is set to be twice as long as the wavelength of the fastest-growing mode of the KH billow estimated from the linear stability theory (e.g., Hazel 1972) to allow for pairing (Klaassen and Peltier 1989). Following Klaassen and Peltier (1991), we take the domain width L_y to be larger than the half-wavelength of one KH billow (quarter of L_x), and the domain height L_z is taken to be larger than the wavelength of one KH billow. We confirm that vertical boundaries do not suppress the pairing and breakdown of billows in all runs.

b. Numerical methods

Spatial discretization is performed via the Fourier pseudospectral method. Time stepping is accomplished using a third-order Adams–Bashforth method, except for the viscosity and diffusion terms, which are evolved analytically. Grid spacing is isotropic and designed to resolve turbulence due to the breakdown of KH billows (Table 1). Further details of the DNS model are found in Smyth et al. (2005).

c. Forcing and tilting angle

A thin layer of strong density stratification supports horizontally propagating waves with frequency $\omega = \sqrt{g'k/2}$ (e.g., Kundu and Cohen 2008). Here, g' is the reduced gravity and k is the horizontal wavenumber. The wavelength is assumed to be large compared with the interface half-thickness h , so that $kh \ll 1$. Considering now the nonzero thickness of the interface, we can replace g' with hN^2 and obtain

$$\frac{\omega}{N} = \sqrt{\frac{kh}{2}}. \quad (5)$$

If the wave-driven shear across the interface is strong enough to support shear instability, the resulting Kelvin–Helmholtz billows will have wavenumber $\tilde{k} \approx 0.5/h$, independent of the shear (e.g., Hazel 1972). Therefore,

TABLE 1. Parameters and results for numerical simulations. Here, Ri_{\min} is the projected minimum Richardson number; ω/N is the normalized forcing frequency; Re_0 is the projected Reynolds number; a is the maximum tilt angle ($^\circ$); b is the amplitude factor for the initial perturbation; $N_x, N_y,$ and N_z are coarse-component grid numbers, where the grid numbers are doubled for a scalar variable; Re_c is the cumulative buoyancy Reynolds number; Mn_c is the cumulative normalized diapycnal flux; Γ_c is the cumulative mixing efficiency; $[R_{OT}]$ is the ratio of the time-averaged Ozmidov scale to the Thorpe scale; and $[R_{BT}]^2$ is the squared ratio of the time-averaged buoyancy length scale to the Thorpe scale.

Run	Ri_{\min}	ω/N	Re_0	a	b	$N_x \times N_y \times N_z$	Re_c	Mn_c	Γ_c	$[R_{OT}]$	$[R_{BT}]^2$	Pairing
AD1	0.07	0.05	300	5.42	0.1	$256 \times 64 \times 128$	11.16	24.16	0.31	0.49	0.08	○
AD2	0.07	0.06	300	6.51	0.1	$256 \times 64 \times 128$	9.18	20.25	0.32	0.44	0.06	○
AD3	0.07	0.07	300	7.59	0.1	$256 \times 64 \times 128$	8.21	19.12	0.33	0.42	0.06	○
AD4	0.07	0.08	300	8.68	0.1	$256 \times 64 \times 128$	7.08	15.04	0.30	0.43	0.06	○
AD5	0.07	0.09	300	9.78	0.1	$256 \times 64 \times 128$	5.63	13.54	0.34	0.47	0.07	×
AD6	0.07	0.10	300	10.87	0.1	$256 \times 64 \times 128$	5.56	12.99	0.33	0.49	0.08	×
AD7	0.08	0.05	300	5.06	0.1	$256 \times 64 \times 128$	4.98	9.18	0.26	0.47	0.06	○
AD8	0.08	0.06	300	6.08	0.1	$256 \times 64 \times 128$	4.11	7.70	0.27	0.48	0.06	○
AD9	0.08	0.065	300	6.59	0.1	$256 \times 64 \times 128$	3.58	7.16	0.29	0.47	0.06	○
AD10	0.08	0.07	300	7.10	0.1	$256 \times 64 \times 128$	3.15	6.99	0.32	0.49	0.07	×
AD11	0.08	0.08	300	8.12	0.1	$256 \times 64 \times 128$	3.16	7.03	0.32	0.48	0.07	×
AD12	0.08	0.09	300	9.14	0.1	$256 \times 64 \times 128$	2.73	5.83	0.31	0.50	0.08	×
AD13	0.08	0.10	300	10.16	0.1	$256 \times 64 \times 128$	2.19	4.77	0.31	0.49	0.07	×
AD14	0.09	0.05	300	4.78	0.1	$256 \times 64 \times 128$	1.59	3.07	0.28	0.48	0.06	×
AD15	0.09	0.06	300	5.74	0.1	$256 \times 64 \times 128$	1.61	3.38	0.30	0.47	0.07	×
AD16	0.09	0.07	300	6.69	0.1	$256 \times 64 \times 128$	1.53	3.22	0.30	0.47	0.07	×
A1	0.08	0.05	300	5.06	0.1	$256 \times 64 \times 128$	11.43	18.14	0.23	0.54	0.07	○
ADR1	0.08	0.07	500	7.10	0.1	$320 \times 80 \times 160$	11.16	26.31	0.34	0.40	0.05	○
ADR2	0.08	0.07	800	7.10	0.1	$384 \times 96 \times 192$	30.62	77.53	0.36	0.44	0.07	○
AD-	0.08	0.07	300	7.10	0.05	$256 \times 64 \times 128$	1.73	3.94	0.33	0.45	0.07	×
AD+	0.08	0.07	300	7.10	0.2	$256 \times 64 \times 128$	5.71	10.59	0.26	0.50	0.07	○
ADR+	0.08	0.05	500	5.06	0.2	$320 \times 80 \times 160$	18.20	42.92	0.34	0.47	0.07	○
AR+	0.08	0.05	500	5.06	0.2	$320 \times 80 \times 160$	25.20	55.18	0.31	0.58	0.11	○
ADRL+	0.03	0.025	500	4.14	0.2	$320 \times 80 \times 160$	26.33	42.59	0.23	0.77	0.14	○
AD7x	0.08	0.05	300	5.06	0.1	$128 \times 64 \times 128$	2.43	5.41	0.32	0.43	0.06	×
ADL+	0.03	0.025	325	4.14	0.2	$256 \times 64 \times 128$	21.94	32.28	0.21	0.87	0.16	×
ADRI+	0.05	0.035	500	4.49	0.2	$320 \times 80 \times 160$	31.21	63.02	0.29	0.64	0.12	○

$$\frac{k}{\bar{k}} \approx 4 \frac{\omega^2}{N^2}. \tag{6}$$

As long as $\omega/N \ll 1$, the wavelength of the gravity wave is much greater than the billow wavelength, so that the horizontal variation of the gravity wave may be neglected. In this case the wave can be represented by a parallel shear layer in which the amplitude of the shear varies in time. Here, that time-varying shear flow is generated by tilting the coordinate system as described in section 2a. We now describe the tilting function and the effect it has on the evolution of the initial state.

As discussed by Thorpe (1968, 1971), the horizontally averaged mean flow \bar{u} in a tilted tank with a laterally periodic boundary condition without the onset of billows is driven by buoyancy in accordance with

$$\frac{\partial \bar{u}}{\partial t} = -g \frac{\bar{\rho}}{\rho_0} \sin \tau, \tag{7}$$

neglecting momentum fluxes due to instability and molecular viscosity. The horizontally averaged density

is denoted by $\bar{\rho}$. In the present experiments, the tilt angle depends sinusoidally on time:

$$\tau = a \sin \omega t, \tag{8}$$

with maximum amplitude a and frequency ω .

At $t = 0$, the density anomaly has a two-layer form, where the layers are separated by a transition zone of thickness $2h_0$:

$$\bar{\rho} = -\Delta\rho \tanh \frac{z}{h_0}, \tag{9}$$

where $\Delta\rho$ is the density change across h_0 . As the tilt angle τ departs from zero, buoyancy generates a sheared velocity profile:

$$\bar{u} = \Delta u(t) \tanh \frac{z}{h_0}, \tag{10}$$

where $\Delta u(t)$ is the velocity change across h_0 . Combining (7)–(10) and expanding $\sin \tau$ in powers of a , we have

$$\Delta u(t) \approx -g \frac{\Delta \rho}{\rho_0} \frac{a}{\omega} (1 - \cos \omega t) + O(a^3). \quad (11)$$

As the shear increases, the minimum Richardson number drops from infinity, eventually becoming smaller than 1/4, at which time the flow becomes unstable and the transition to turbulence begins. As discussed in section 1, we evaluate the mixing efficiency Γ as a function of two dimensionless outer parameters: the ratio of the tilting frequency to the buoyancy frequency ω/N and the projected minimum Richardson number Ri_{\min} (Table 1), where Ri_{\min} is the minimum value of the Richardson number achieved in the absence of viscosity and instability (i.e., due to forcing alone) at the interface and $\omega t = \pi$. By differentiating (7), Ri can be related to the tilting angle τ as

$$\text{Ri} = \frac{N^2}{\left(\frac{\partial \bar{u}}{\partial z}\right)^2} = \frac{\cos \tau}{N^2 \left(\int_0^t \sin \tau dt\right)^2}. \quad (12)$$

See Thorpe (1971) for further details. If we make the small angle approximation $a \ll 1$, we obtain

$$\text{Ri}_{\min} \approx \frac{\omega^2}{4a^2 N^2}. \quad (13)$$

From this we see that Ri_{\min} expresses the strength of the forcing, as it is inversely proportional to a^2 for given ω/N . Its value also gives us an initial indication of the potential for KH instability in a given experiment. In planning these simulations, we choose a value for Ri_{\min} and ω/N , then compute the necessary maximum tilt angle a . Rather than using (13), we invert (12) numerically, thereby avoiding the small inaccuracy due to the small angle approximation.

d. Initial conditions and termination criteria

The projected Reynolds number is defined for the flow state in which $\text{Ri} = \text{Ri}_{\min}$:

$$\text{Re}_0 = \frac{h_0 \Delta u}{\nu}. \quad (14)$$

Here, Δu is the value of the half-velocity change that gives $\text{Ri} = \text{Ri}_{\min}$. Once Re_0 is chosen, (14) gives a value for the initial half-layer thickness h_0 . Molecular effects on the mean flow cause the layer thickness to increase slowly from this initial value. To minimize computational time and interface thickening, we start numerical runs when Ri first decreases to 0.25, the critical value for instability. This is arranged by using (9) and (10) for the initial condition, with Δu chosen so that $\text{Ri} = 0.25$. For most of the experiments reported here, we choose

$\text{Re}_0 = 300$. The effects of different Re_0 are discussed in section 4d.

We use the reference buoyancy frequency N_0 for dimensionless time, $t_{nd} = N_0 t / (2\pi)$:

$$N_0 = \text{Ri}_{\min}^{1/2} \frac{\Delta u}{h_0}. \quad (15)$$

We also add a disturbance to the initial profiles to efficiently reproduce the three-dimensional motion (Smyth et al. 2005). The perturbation consists of a random velocity field concentrated near $z = 0$ and having its maximum amplitude equal to $b\Delta u$, in which the constant b is a dimensionless measure of the noise amplitude (Table 1). The effects of different amplitudes are discussed in section 4d.

Nondimensional domain lengths for the streamwise, spanwise, and vertical directions are $L_x/(2h_0) = 13.96$, $L/(2h_0) = 3.49$, and $L_z/(2h_0) = 6.98$, respectively. We anticipate that acceleration phases subsequent to $\omega t = 2\pi$ may drive additional mixing; however, by $\omega t = 2\pi$, the transition layer has invariably thickened so that billows emerging in later acceleration phases will have significantly increased wavelength. As a result, the domain dimension chosen to accommodate the initial instability will no longer be appropriate. For this reason, we terminate all simulations no later than $\omega t = 2\pi$. In some cases where the forcing time scale is very long, mixing is complete before ωt reaches the final value 2π . For economy, these runs are terminated when the intensity of the scalar mixing becomes the molecular level.

3. Mixing diagnostics

The volume-averaged kinetic energy \mathcal{K} and potential energy \mathcal{P} are defined as

$$\mathcal{K} = \frac{1}{2} \langle \mathbf{u} \cdot \mathbf{u} \rangle_V, \quad \mathcal{P} = \frac{g}{\rho_0} \langle \rho z \rangle_V, \quad (16)$$

where $\langle \rangle_V$ is the average over the computational domain. The volume-averaged energy budget for stratified turbulence can be written as

$$\frac{d\mathcal{K}}{dt} = -\mathcal{B} - \varepsilon, \quad (17)$$

$$\frac{d\mathcal{P}}{dt} = \mathcal{B} + \Phi. \quad (18)$$

The buoyancy flux is denoted by \mathcal{B} and ε is the kinetic energy dissipation rate. In addition, Φ is the irreversible changing rate of \mathcal{P} due to the molecular diffusion of the instantaneous linear density profile:

$$\Phi = \frac{\nu}{\text{Pr}} \frac{g \cos \tau \Delta \rho}{\rho_0 L_z}. \quad (19)$$

We also subdivide the potential energy into its available potential energy \mathcal{P}_a and background potential energy \mathcal{P}_b as

$$\mathcal{P} = \mathcal{P}_a + \mathcal{P}_b, \quad (20)$$

where

$$\mathcal{P}_b = \frac{g}{\rho_0} \langle \rho_b z \rangle_V. \quad (21)$$

Here, ρ_b represents the background density profile obtained by using the three-dimensional reordered density and is the density profile of the minimum potential energy state; therefore, its change is due to irreversible mixing processes (Winters et al. 1995). We compute \mathcal{P}_a as

$$\mathcal{P}_a = \mathcal{P} - \mathcal{P}_b. \quad (22)$$

The changing rate of the potential energy can be subdivided into two components, and the background density profile is related to irreversible mixing processes (Winters et al. 1995):

$$\frac{d\mathcal{P}_a}{dt} = \mathcal{B} - \mathcal{M}, \quad (23)$$

$$\frac{d\mathcal{P}_b}{dt} = \mathcal{M} + \Phi. \quad (24)$$

Here, \mathcal{P}_a exchanges energy with \mathcal{K} via \mathcal{B} , and \mathcal{M} is the changing rate of the background potential energy due to the turbulent diapycnal mixing:

$$\mathcal{M} = \frac{d\mathcal{P}_b}{dt} - \Phi = \frac{g}{\rho_0} \frac{d\langle \rho_b z \rangle_V}{dt} - \Phi. \quad (25)$$

The instantaneous ratio of the turbulent diapycnal flux to ε' is defined (Carpenter et al. 2007; Smyth et al. 2007) as

$$\Gamma_i = \frac{\mathcal{M}}{\varepsilon'}. \quad (26)$$

Here, ε' is the dissipation rate due to velocity fluctuations, defined by $\mathbf{u}' = \mathbf{u} - \bar{\mathbf{u}}$, where $\bar{\mathbf{u}} = (\bar{u}, 0, 0)$ and could correspond to oceanic measurements (a detailed explanation is found in Smyth et al. 2007). Since high Γ_i does not necessarily mean large flux or intense mixing, we also use normalized \mathcal{M} ($\mathcal{M}n$) and ε' (Re) for comparison:

$$\mathcal{M}n_i = \frac{\mathcal{M}}{\Phi}, \quad \text{Re}_i = \frac{\varepsilon'}{\text{Pr}\Phi}. \quad (27)$$

These expressions for the diagnostics are only strictly correct at times when the tilt angle is zero; however, we evaluate it continuously in time to facilitate comparison with previous studies. Ambiguities involved with the

diagnostics in the tilting frame are discussed in the appendix.

Net mixing parameters for each run are computed as

$$\text{Re}_c = \frac{\int_{t_1}^{t_2} \varepsilon' dt}{\text{Pr} \int_{t_1}^{t_2} \Phi dt}, \quad \mathcal{M}n_c = \frac{\int_{t_1}^{t_2} \mathcal{M} dt}{\int_{t_1}^{t_2} \Phi dt}, \quad \Gamma_c = \frac{\int_{t_1}^{t_2} \mathcal{M} dt}{\int_{t_1}^{t_2} \varepsilon' dt}, \quad (28)$$

where t_1 is defined as the time when the first turbulent diapycnal flux (25) increases to the same magnitude as that due to the molecular diffusion (19), $\mathcal{M}n_i > 1$, and $t_2 = 2\pi/\omega$. If the forcing frequency is small, then the turbulent mixing decreases to the molecular diffusion level before one forcing cycle is achieved. In those cases, we define t_2 as the time just before $\mathcal{M}n_i < 1$. We mainly examine these time-averaged values because this allows us to ignore time dependence and may also correspond to the average of many samples randomly observed in the ocean.

4. Results

Here, we explain how Γ_c depends on forcing fields. First, we connect our work with previous studies by showing how mixing is suppressed in the deceleration phase. Second, we investigate the dependences of Γ_c on Ri_{\min} and ω/N with fixed Re_0 and b . Third, we explain further the dependences of Γ_c on Re_0 and b . Last, we focus on low-frequency forcing fields with higher Re_0 .

a. Effects of mean flow deceleration

The present experiments differ from previous simulations of the unforced case (e.g., Smyth et al. 2001) mainly because the mean shear that drives instability exists only for a limited time before it is decelerated by the external forcing. The mean flow is accelerated from the beginning of the run until $\omega t = \pi$, and then decelerated from $\omega t = \pi$ to $\omega t = 2\pi$. Note that the mean flow does not change sign. In the acceleration phase, KH billows grow much as they do in the unforced case. The subsequent deceleration, however, can have dramatic effects on the disturbance evolution as it reduces the mean flow kinetic energy available to drive the disturbance. We examine the effects of the deceleration phase by comparing runs with and without deceleration. To omit deceleration, we simply leave the tilt angle (8) as zero for $\omega t > \pi$.

Figure 1 shows the results for the cases with $\text{Ri}_{\min} = 0.08$ and $\omega/N = 0.05$ (AD7 and A1 in Table 1). After Ri drops below $1/4$, a train of KH billows emerges. The computational domain accommodates two such billows as shown in Fig. 1a. The billows pair (Fig. 1b), then

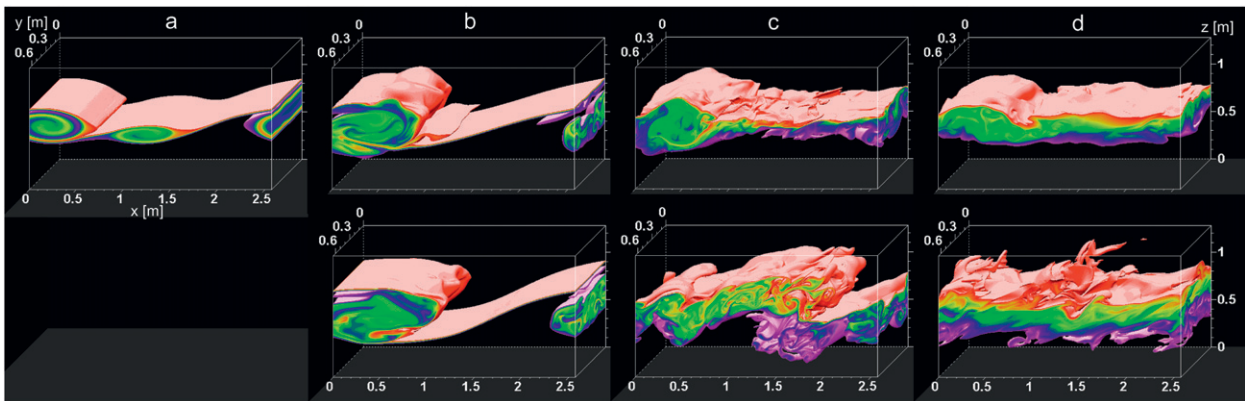


FIG. 1. Density field for KH billows forced (top) with (AD7) and (bottom) without (A1) a deceleration phase. Colored values cover the middle three-fifths of the density range; higher and lower values are transparent. The actual domain length in the computation is used for the axes: $t_{nd} =$ (a) 11.1, (b) 12.8, (c) 14.4, and (d) 16.3.

break and become turbulent (Figs. 1c and 1d). The effect of deceleration is clear in Fig. 1c. With no deceleration phase (A1, bottom frames in Fig. 1), the paired KH billow is sheared into two parts by the strong mean flow. With deceleration (AD7), the billow relaxes to a more circular shape. As the mean flow decelerates toward zero, the billow collapses into a field of weakly turbulent gravity waves (Fig. 1d, top), whereas without deceleration (A1), the mean shear generates sustained turbulence (Fig. 1d, bottom).

Energy budgets can help to explain these mixing events. KH instability occurs after the acceleration (Fig. 2a); during this weakly nonlinear regime, the mean flow is diminished due to deceleration and ceases to support the KH billows. Thus, the maximum potential energy is diminished between $t_{nd} = 12$ and 13 (Fig. 2b). The subsequent turbulence Re_i after $t_{nd} = 13$ is also diminished as is the diapycnal flux $\mathcal{M}n_i$ (Figs. 2c and 2d). AD7 has maximum values of Re_i and $\mathcal{M}n_i$ after breakdown at $t_{nd} = 13.4$. However, there is a time lag in A1 ($t_{nd} = 14$ in Fig. 2c and $t_{nd} = 13.7$ in Fig. 2d) because the secondary instability of the KH billows (Klaassen and Peltier 1985) results in maximum $\mathcal{M}n_i$ during breakdown. The difference in Γ_i seems small in Fig. 2e. Before breakdown ($t_{nd} < 12$), $\Gamma_i \approx 0.7$ corresponds to highly efficient preturbulent mixing (Smyth et al. 2001). In the turbulence stage, $\Gamma_i \approx 0.2$ is achieved and the mixing in A1 lasts longer. Contributions to the diapycnal flux from the preturbulent phase are more important in AD7 because deceleration suppresses turbulence at later times. Cumulative values have differences due to the different intensities and durations of the preturbulent and turbulent phases: $Re_c = 4.98$ (11.43), $\mathcal{M}n_c = 9.18$ (18.14), and $\Gamma_c = 0.26$ (0.23) for AD7 (A1). In AD7, the values of Re_c are less than half of that in A1, suggesting strong modification due to a deceleration phase.

If Ri_{\min} is larger, KH billows will grow more slowly (e.g., Hazel 1972) and be suppressed by mean flow deceleration. If ω/N is larger, the faster arrival of the deceleration will suppress the growth of the KH billows. Therefore, the relative timing of the billow growth and mean flow deceleration will be important for a mixing event.

b. High-frequency forcing

In the classic observations of Woods (1968), KH billows were generated by gravity waves propagating on thin layers of strong stratification and were related to existing theories of shear instability (Miles and Howard 1964). The observed gravity waves had wavelength $\lambda \approx 10$ m and the thickness of the interface was $2h \approx 0.1$ m. Using (5), the normalized frequency of the observed waves can be estimated as $\omega/N \sim 0.1$. Although our wavelike forcing does not strictly correspond to interfacial gravity waves, we choose $\omega/N = 0.1$ as a reference with $Ri_{\min} = 0.07$ (AD6) and 0.08 (AD13) corresponding to the lower limit of Richardson number in Woods (1968) (Fig. 3 and Table 1). When Ri_{\min} is larger than this, there is no full development of KH billows due to the slower growth of the billows. Then, $\mathcal{M}n_c$ becomes close to 1 (molecular value); thus, mixing due to shear instability is negligible (Fig. 4).

In both cases, the deceleration phase of the high-frequency forcing strongly affects the initial growth of the KH billows (Fig. 4) and there is no pairing. Mixing is not completed within one forcing cycle. Both Re_c and $\mathcal{M}n_c$ are small (Fig. 3), but Γ_c is higher (≥ 0.3) because the efficient preturbulent mixing (Smyth et al. 2001) contributes significantly to the net diapycnal flux. At low Ri_{\min} (AD6), preturbulent mixing is intense and Γ_c is higher (Fig. 4).

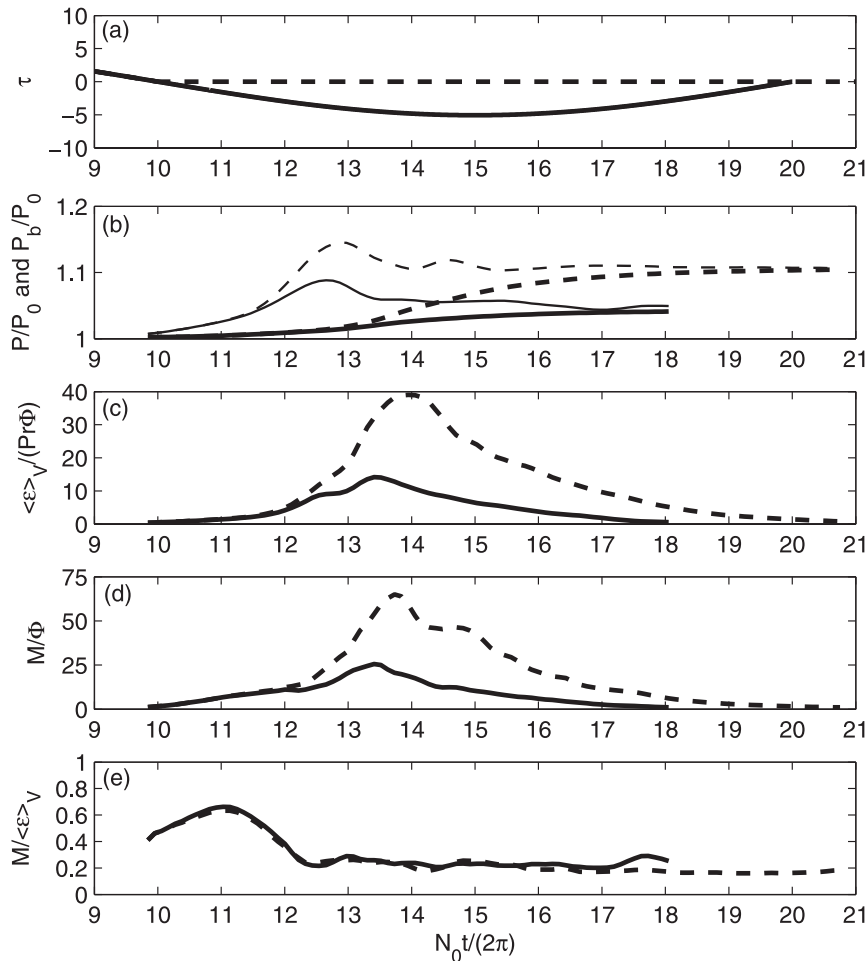


FIG. 2. Time series of a DNS run ($Ri_{\min} = 0.08$ and $\omega/N = 0.05$). The solid line shows the run with a deceleration phase (AD7) and the dashed line that without deceleration (A1). The horizontal axis is dimensionless in time. Shown are the (a) tilting angle, (b) total (thin line) and background (thick line) potential energies normalized by $\mathcal{P}_0 = g/\rho_0 \langle \bar{\rho}z \rangle_z$, (c) instantaneous dimensionless kinetic energy dissipation rate Re_i , (d) instantaneous dimensionless diapycnal buoyancy flux $\mathcal{M}n_i$, and (e) instantaneous ratio of diapycnal buoyancy flux to kinetic energy dissipation rate Γ_i .

c. Effects of decreased forcing frequency

The assumption that the maximum tilt angle a is small is necessary for some elements of our analysis, and is also well justified by the fact that even strongly nonlinear interfacial waves in the ocean usually have steepness that is much less than unity (e.g., Moum et al. 2003). Assuming $a \ll 1$ in (13) implies

$$\frac{\omega}{N} \ll 2\sqrt{Ri_{\min}}. \quad (29)$$

Combining this with the requirement for instability, $Ri_{\min} < 1/4$, we find that the assumption of small tilt angle is equivalent to $\omega/N \ll 1$. The condition of low steepness, combined with the condition for instability, is

therefore equivalent to a requirement that the wave frequency be much smaller than the buoyancy frequency. The observed waves discussed in section 4b had $\omega/N \sim O(0.1)$, and therefore satisfied this criterion marginally. In the remainder of this study, we will focus on cases with $\omega/N < 0.1$.

In our parameter space (Fig. 3), smaller Ri_{\min} or smaller ω/N tends to make larger Re_c and $\mathcal{M}n_c$ because of the faster growth of KH billows or slower arrival of deceleration. When Ri_{\min} is larger and ω/N is smaller, it takes a longer time before the onset and an interface are diffused via molecular processes. The thickness of the velocity interface becomes greater than that of the density interface due to different diffusivities; therefore, the projected Ri_{\min} from (12) will not work well and

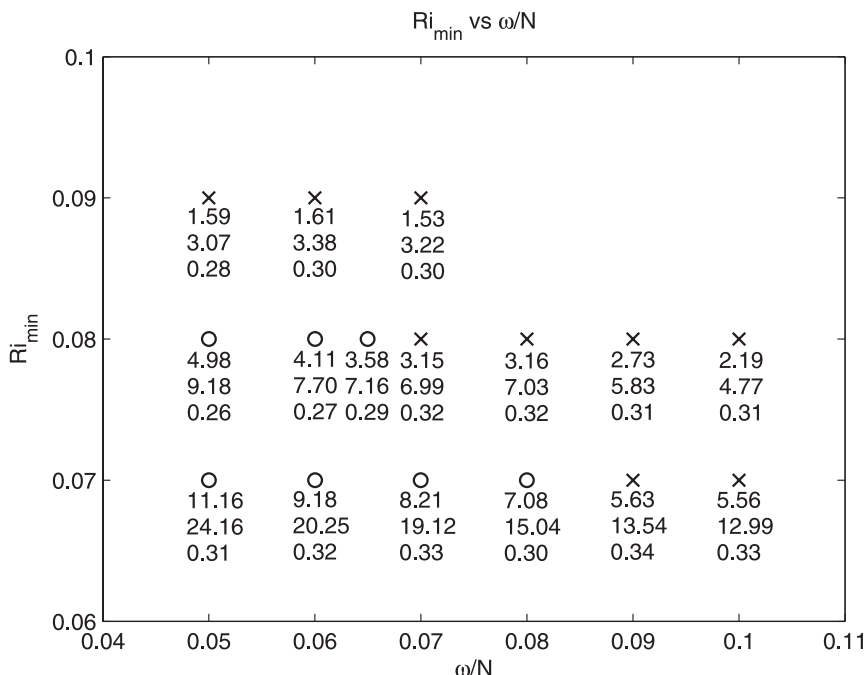


FIG. 3. Results in Ri_{min} and ω/N spaces for $Re_0 = 300$. Numbers in columns show the cumulative buoyancy Reynolds number Re_c , cumulative dimensionless diapycnal flux due to mixing Mn_c , and cumulative mixing efficiency Γ_c . Pairing is observed at the open circle and not at the cross.

Holmboe instability (Holmboe 1962) may occur. This is most likely in low- Re_0 cases (Fig. 4).

Over the range of parameter values shown in Fig. 3, Γ_c remains within about 20% of 0.3. When preturbulent mixing is important and turbulence is suppressed by the deceleration phase, as mentioned in section 4b, Γ_c is higher. When Ri_{min} is smaller, this higher Γ_c appears at larger ω/N because Γ_c is controlled by the relative timing of two events: the growth of KH billows and the arrival of the deceleration phase. The boundary between the pairing and nonpairing cases seems to be defined by this relative timing (Fig. 3). This is analogous to the boundary between the mixing and nonmixing cases, because the pairing instability is the subharmonic mode of the primary KH instability (e.g., Klaassen and Peltier 1989). For $Ri_{min} = 0.07$ and $\omega/N = 0.07$ (AD3 in Table 1), KH billows can grow faster and pair, then deceleration suppresses turbulence and makes Γ_c higher.

If both Ri_{min} and ω/N are small, we could expect that a mixing event may be completed within the acceleration phase (Fig. 4). We further explore this situation with different initial conditions and will show that $\Gamma_c \approx 0.2$. In preparation for this, we first examine the effects of different projected Reynolds numbers Re_0 and the amplitude of the initial perturbation b showing that higher Re_0 and b intensify the development of KH bil-

lows and allow us to avoid the interface thickening in the low-frequency forcing.

d. Sensitivity to Re_0 and b

In addition to Ri_{min} and ω/N , Γ_c depends on the projected Reynolds number Re_0 and the amplitude of the initial perturbation b . Furthermore, the fact that the

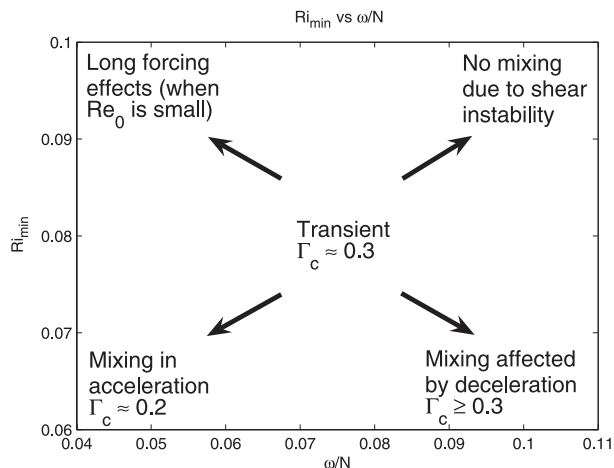


FIG. 4. Schematic in Ri_{min} and ω/N space.

value for Re_0 used in our DNS is smaller than typical oceanic values gives some doubt as to the generality of our results for the ocean. To examine the sensitivity to these additional parameters, we add DNS runs with different values of the projected $Re_0 = 500$ (ADR1) and $Re_0 = 800$ (ADR2) and different b (AD- with $b = 0.05$ and AD+ with $b = 0.2$) in Table 1. We use $Ri_{\min} = 0.08$ and $\omega/N = 0.07$, where the deceleration has a significant effect on the mixing at $Re_0 = 300$ (Fig. 3 and AD10 in Table 1).

As Re_0 becomes higher, KH billows grow faster and pairing can occur. Higher Re_0 can accelerate secondary instability (Klaassen and Peltier 1985); therefore, efficient mixing during pairing and breakdown is enhanced and is stronger than in $Re_0 = 300$ runs (Table 1). ADR2 has the larger Γ_c (Table 1) because the deceleration suppresses mixing just after breakdown. Although mixing continues after one forcing cycle in higher Re_0 runs, tilting is stopped after one forcing cycle.

For AD-, the smaller initial disturbance amplitude b makes the onset slower; thus, mixing is suppressed by deceleration at an earlier phase in billow evolution. For AD+, the larger b makes the onset faster than AD10 and promotes pairing and subsequent intense, and less efficient, turbulence. Thus, the effects of preturbulent mixing become less. This reduced importance of preturbulent mixing is also found in Holmboe wave simulations (Smyth et al. 2007). The result is that Γ_c becomes smaller and the intensity of the mixing is similar to that in AD7.

Next, we conduct the higher $Re_0 = 500$, larger $b = 0.2$, and longer duration of forcing ($\omega/N = 0.05$) runs (with deceleration, ADR+, and without deceleration, AR+, in Table 1) to see whether the effects of deceleration are reduced. KH billows start to develop at $t_{nd} = 9.5$. There is a little difference in the maximum potential energy in the developing stage because billows can grow before the deceleration affects the mixing (Fig. 5b). During and after breakdown, Re_i is high because of the faster growth of the secondary instability ($12 < t_{nd} < 13$ in Fig. 5c); Mn_i becomes high around breakdown because of higher Re_i and $\Gamma_i \approx 0.4$ ($12 < t_{nd} < 13$ in Figs. 5d and 5e). The highest Γ_i in the initial rollup of the KH billows does not contribute much to the diapycnal flux. However, the efficient mixing around breakdown is more important in the higher- Re_0 case. In the decaying turbulence stage, Γ_i decreases to 0.2 (Fig. 5e). The effect of deceleration appears after $t_{nd} = 12$ but seems less important than that shown in Fig. 2 (AD7 and A1) and mixing in ADR+ lasts longer than AD7. We see in Table 1 that Re_c , Mn_c , and Γ_c become 18.20 (25.20), 42.92 (55.18) and 0.34 (0.31) for ADR+ (AR+). It is also apparent that Γ_c is higher than 0.3 due to efficient mixing around breakdown and ADR+ has higher Γ_c

because of the deceleration. Since these differences in the cumulative values between these runs are smaller than those discussed in section 4a, the deceleration phase appears to become less important if ω/N is smaller and Re_0 is higher. In ADR+, the Γ_c increase is 30% larger than in AD7, showing the dependence on Re_0 because mixing during breakdown is more efficient in higher Re_0 .

e. Highly unstable, low-frequency forcing

When both Ri_{\min} and ω/N are small, mixing by fully developed turbulence is not suppressed by the deceleration, and we therefore expect to recover the canonical turbulent mixing efficiency $\Gamma_c = 0.2$. To test this speculation, we examine a case with low $Ri_{\min} = 0.03$ and low $\omega/N = 0.025$. We also use increased values of Re_0 and b to promote the rapid onset of turbulence (ADRL+ in Table 1).

KH billows start to develop and break before Ri_{\min} is achieved ($t_{nd} < 15$ in Figs. 6a and 6b). Intense mixing is almost completed before deceleration begins at $t_{nd} = 20$ (Figs. 6c and 6d). Because onset occurs during acceleration, the maximum potential energy is larger than before ($t_{nd} = 14.2$ in Fig. 6b). Turbulence becomes intense after breakdown and the maximum value is achieved after breakdown ($t_{nd} > 16$ in Fig. 6c). However, the larger Mn_i (Fig. 6d) has two causes. One is the high diapycnal flux during breakdown with higher $\Gamma_i (> 0.4)$ (Fig. 6e) as before. The other is flux after breakdown with larger Re_i with $\Gamma_i \approx 0.2$ (Fig. 6e) due to turbulence. Because the forcing keeps accelerating the mean shear, less efficient mixing ($\Gamma_i = 0.2$) continues longer until the end of the event and cancels the higher Γ_i around breakdown. Here P_b/P_0 suggests that roughly 15% of total potential energy gain is achieved before breakdown at $t_{nd} = 15.2$ (Fig. 6b). This ratio is smaller than the higher ω/N case (around 30% in Fig. 5b) where highly efficient mixing during breakdown is important. We note that the acceleration during breakdown makes mixing more efficient (Γ_i up to 0.6 at $t_{nd} = 15$) than that during pairing ($t_{nd} = 13$) in Fig. 6e. Even though the efficient mixing is reproduced in this higher Re_0 run, Γ_c is near 0.2 (Table 1).

From the above results, we may infer ocean mixing that is due to a low-frequency wave with high Reynolds number as follows. The high Reynolds number can accelerate the onset of KH billows and the subsequent transition to turbulence. This process leads to efficient and intense mixing around breakdown, but this faster transition also makes the duration of turbulence longer, which tends to cancel the efficient mixing. Finally, mixing efficiency becomes ≈ 0.2 . The lack of this long duration of turbulence may explain why both laboratory

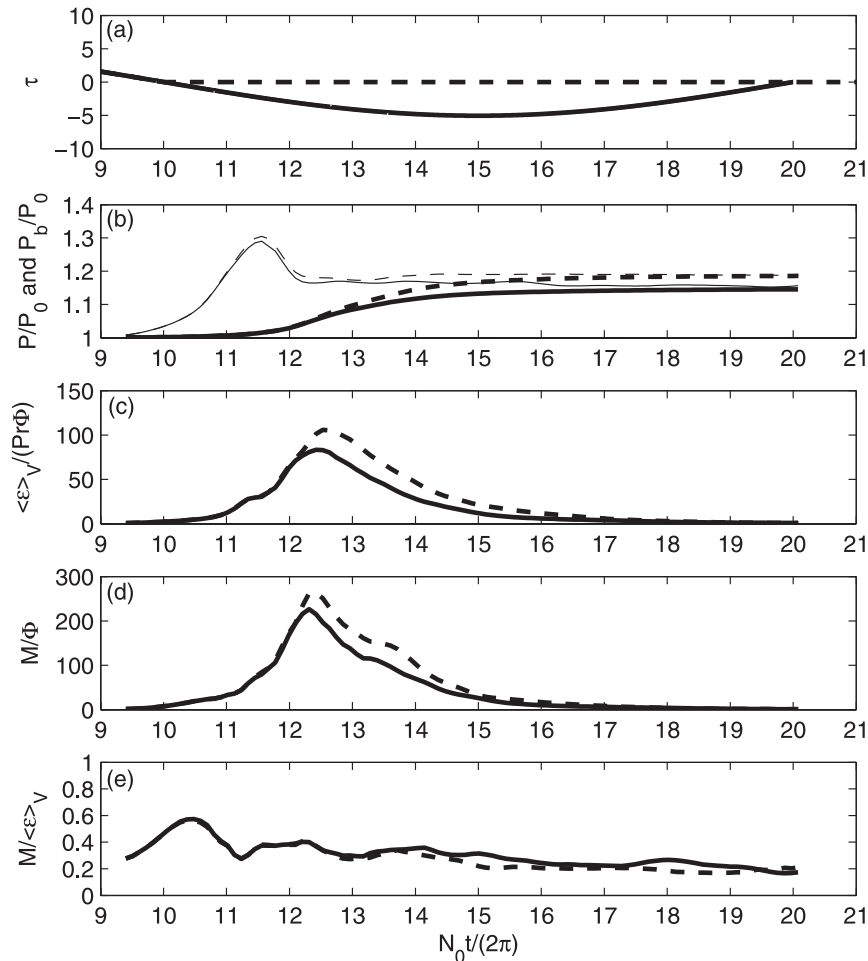


FIG. 5. Same as in Fig. 2, but for $Ri_{\min} = 0.08$ and $\omega/N = 0.05$ with higher $Re_0 = 500$ and $b = 0.2$. Solid line shows the run with a deceleration phase and dashed line shows that without deceleration.

experiments (Thorpe 1973) and DNS (e.g., Smyth et al. 2001) had higher mixing efficiency ($\Gamma_c \geq 0.3$). We may need to be careful not to assume 0.2 for the ocean mixing forced by high-frequency internal waves, because in that case a large fraction of the mixing can be accomplished in the highly efficient preturbulent phase.

We note that, in the longer forcing run, there could be an additional pairing if our boundary conditions allowed it, and that could alter the value of Γ_c . To simulate this would require more memory than is available. Instead, we address the issue indirectly by examining a case in which the first pairing is suppressed. An auxiliary simulation was conducted with $Ri_{\min} = 0.08$, $\omega/N = 0.05$, and $Re_0 = 300$, similar to AD7, but with L_x halved so as to suppress the pairing (AD7x in Table 1). The result was that Γ_c was increased from 0.26 (AD7) to 0.32 (AD7x) because of the weaker turbulence after breakdown. This indicates that suppression of

pairing results in larger Γ_c . Therefore, if pairing was allowed in ADRL+, we expect that Γ_c would be smaller.

We add two runs to see the effects of forcing parameters on the above results. One run has the same parameters except smaller $Re_0 (= 325)$ (ADL+ in Table 1). The other run has an intermediate $Ri_{\min} (= 0.05)$ and $\omega/N (= 0.035)$ with the same $Re_0 (= 500)$ (ADRI+ in Table 1) to see effects of Ri_{\min} and ω/N . In ADL+, the pairing instability is not reproduced and one KH billow is absorbed in the interface [cf. “draining instability” in Klaassen and Peltier (1989)], but forcing accelerates the mean shear during the turbulent phase. We note that $\mathcal{M}n_c$ is smaller than ADRL+ because mixing during breakdown is less efficient in lower Re_0 (Table 1). In these long forcing runs, the effects of Re_0 on Γ_c are small. In ADRI+, the forcing field keeps accelerating the KH billows during breakdown, but the deceleration phase is arrived at faster than for the

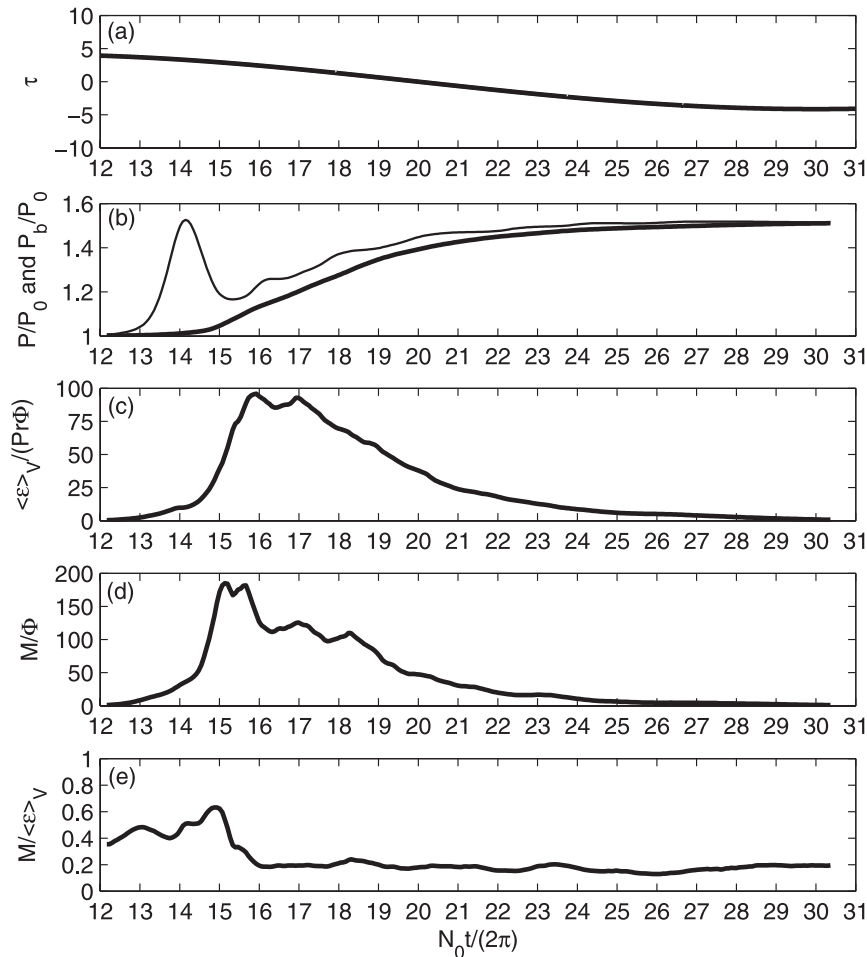


FIG. 6. Same as in Fig. 2, but for $Ri_{\min} = 0.03 \omega/N$ and $= 0.025$ with $Re_0 = 500$ and $b = 0.2$. Only the case with a deceleration phase is shown. The deceleration starts at $N_0 t / (2\pi) = 20$.

$\omega/N = 0.025$ cases. Therefore, the duration of the turbulence is shorter and there is a suppression of turbulence. This run has higher Re_c and $\mathcal{M}n_c$ than ADRL+, possibly because lower Ri is achieved during KH instability due to the higher forcing frequency, and the nonsteadiness of the forcing field becomes important (Table 1). However, Γ_c is higher (0.29) than ADRL+ and ADL+ as expected.

5. Comparison with observations

We have shown that the mixing efficiency depends on forcing, but it is not clear yet whether we can use $\Gamma = 0.2$ in the ocean mixing. Here, we compare the DNS results with microstructure measurements by using a turbulent kinetic energy (TKE) equation averaged over one mixing event. After averaging over an event, we can write the TKE equation following (17) and Smyth et al. (2007) as

$$[\mathcal{S}] = [\mathcal{B}] + [\varepsilon'], \tag{30}$$

where $[\]$ is the average over one event via the same way as (28). Here, \mathcal{S} is the shear production term. By using the time-averaged flux Richardson number, $[Ri_f] = [\mathcal{B}]/[\mathcal{S}] = \Gamma_c / (1 + \Gamma_c)$, where $[\mathcal{B}] = [\mathcal{M}]$, we can rewrite (30) as

$$[\mathcal{B}] = \Gamma_c [\varepsilon']. \tag{31}$$

Then, we introduce two measurable length scales (Dillon 1982; Garrett 2001), the Thorpe scale (L_T) and the Ozmidov scale (L_O), which may be related to KH instability and subsequent mixing in the time-averaged sense. We obtain L_T from the kinematical definition (Thorpe 1977) to estimate the typical parcel vertical displacement, which is defined as the mean square root of the Thorpe displacement δ_T usually in the mixing (or transition) layer:

$$L_T = \langle \delta_T^2 \rangle_{\text{mix}}^{1/2}, \tag{32}$$

where $\langle \rangle_{\text{mix}}$ is the volume average over the mixing layer. In addition, L_O is the length scale at which the turbulence is strongly affected by buoyancy and is defined as (Ozmidov 1965)

$$L_O = \left(\frac{\langle \varepsilon' \rangle_{\text{mix}}}{\langle N_*^3 \rangle_{z_{\text{mix}}}} \right)^{1/2}, \quad (33)$$

where $\langle N_*^3 \rangle_{z_{\text{mix}}}$ is the vertical average of the cubed buoyancy frequency, estimated from the three-dimensional reordered density field within the mixing layer:

$$N_*^2 = -\frac{g \cos \tau}{\rho_0} \frac{d\rho_b}{dz}. \quad (34)$$

In our model, mixing is confined within the transition layer; thus, we define the vertical length (z_{mix}) as

$$z_{\text{mix}}(t) = \max|z_1(x, y, t) - z_2(x, y, t)|, \quad (35)$$

where z_1 and z_2 satisfy $\rho(x, y, z_1, t) = -\Delta\rho \tanh(1)$ and $\rho(x, y, z_2, t) = \Delta\rho \tanh(1)$ (Smyth et al. 2005), respectively. If we further introduce the buoyancy length scale,

$$L_B = \left(\frac{\langle B \rangle_{\text{mix}}}{\langle N_*^3 \rangle_{z_{\text{mix}}}} \right)^{1/2}, \quad (36)$$

(30) becomes

$$[R_{BT}]^2 = \Gamma_c [R_{OT}]^2, \quad (37)$$

where R_{BT} and R_{OT} are the ratio of L_B and L_O to L_T , respectively. Equation (37) suggests that, in the time-average sense, the TKE equation can be described with three dimensionless parameters (R_{BT} , Γ_c , and R_{OT}). Also, R_{OT} is related to our estimation of ε from the reordered density profiles (e.g., Galbraith and Kelley 1996) and is observed to be 0.79 (Dillon 1982) and 0.66 (Crawford 1986). Garrett (2001) proposed $R_{BT}^2 \approx 0.1$. Although these variables are defined in the mixing layer for correspondence with the observations, we use Γ_c that is obtained in the whole domain. All variables need to be averaged over one mixing event, but our DNS is limited to one forcing cycle. The fact that z_{mix} is a function of time may violate the mathematical correctness of the energy budget.

The $[L_O]/h_0$ versus $[L_T]/h_0$ diagram in Fig. 7a describes how the mixing is modified by the forcing. When the rollup of KH billows is suppressed, both $[L_T]/h_0$ and $[L_O]/h_0$ are small. When the pairing instability occurs,

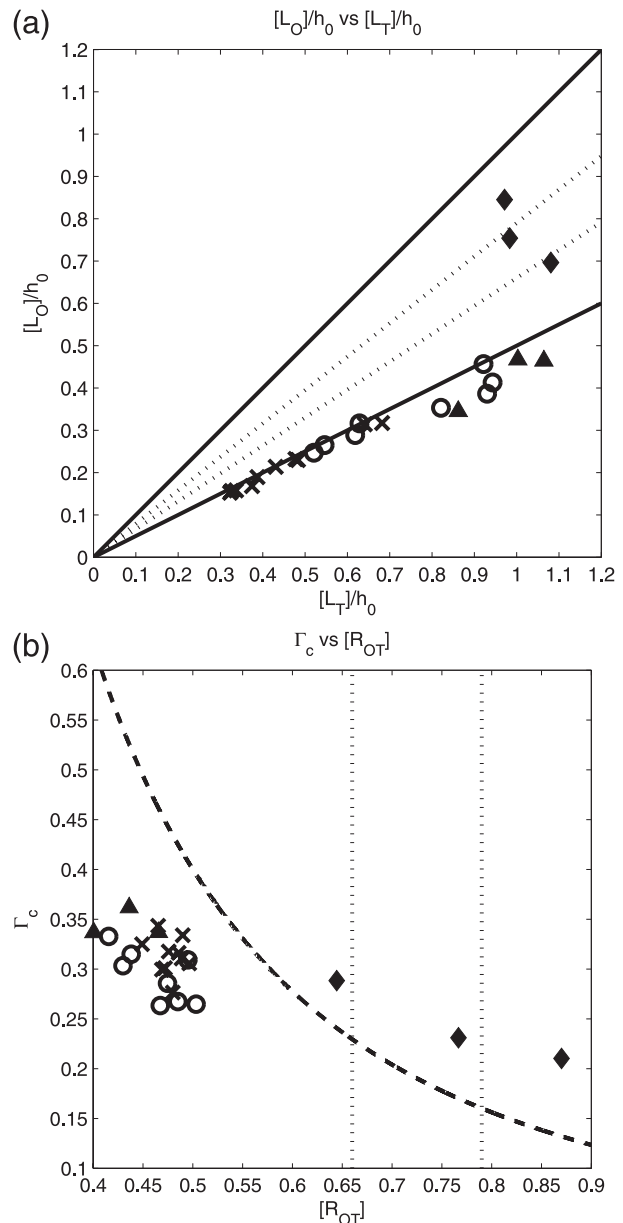


FIG. 7. (a) The $[L_O]/h_0$ vs $[L_T]/h_0$ diagram, and (b) the Γ_c vs $[R_{OT}]$ diagram. Runs with the deceleration phase are plotted. The open circle is $Re_0 = 300$; the pairing is observed (AD1–AD4, AD7–AD9, and AD+). A cross is the same as an open circle but with no pairing (AD5–AD6, AD10–AD16, and AD–). The triangle is for $Re_0 = 500$ or 800 (ADR1, ADR2, and ADR+). Diamonds are for the long forcing cases (ADRL+, ADL+, and ADRI+). Dotted lines are for $R_{OT} = 0.79$ (Dillon 1982) and $R_{OT} = 0.66$ (Crawford 1986). Solid lines in (a) are $R_{OT} = 0.5$ and $R_{OT} = 1.0$. Dashed line in (b) is $R_{BT}^2 = 0.1$, from Garrett (2001).

both $[L_T]/h_0$ and $[L_O]/h_0$ are larger than in the no-pairing cases. However, for some pairing cases, mixing is not completed within one forcing cycle; thus, $[L_T]/h_0$ is large, but $[L_O]/h_0$ is small. Here $[R_{OT}]$ becomes

smaller than for the no-pairing cases. For the long forcing runs, $[L_O]/h_0$ can have larger values within one forcing cycle, then $[R_{OT}]$ is comparable to in situ observations (Dillon 1982; Crawford 1986). In Fig. 7b the Γ_c versus $[R_{OT}]$ diagram also shows the dependences on the forcing fields in terms of the energy budget, as in (37). When the deceleration phase suppresses a mixing event, $[R_{OT}]$ is small and Γ_c is high. The value of $[R_{BT}]^2$ is around 0.07. If deceleration does not suppress turbulence until late in the event, $[R_{OT}]$ is higher, Γ_c is smaller, and $[R_{BT}]^2$ is around 0.15.

These results suggest the importance of the acceleration in the turbulence stage to reproducing the observed values in DNS. Since this scaling shows clear dependences on the forcing fields, application of this scaling to in situ microstructure measurements will be useful for furthering our understanding of the mixing efficiency. The in situ observations could give us some idea of the high Reynolds number turbulence, which we cannot explore by using present-day computers. We also need to compare the statistics of turbulent events and the effects of different sampling methods in the ocean and DNS (e.g., Wijesekera and Dillon 1997; Smyth et al. 2001).

6. Summary

We have investigated the dependence of mixing efficiency on forcing fields via direct numerical simulation (DNS) of Kelvin–Helmholtz (KH) instability. We used a tilted coordinate system to reproduce time-varying forcing fields with a wavelike oscillation, so that the mean shear that drives instability exists only for a limited time before it is decelerated. The cumulative mixing efficiency Γ_c is defined as buoyancy flux as a fraction of the energy dissipation rate, both averaged over one forcing cycle. We described Γ_c as a function of the projected minimum Richardson number Ri_{\min} , the normalized forcing frequency ω/N , the projected Reynolds number Re_0 , and the amplitude of the initial perturbation b . We showed sensitivities of Γ_c on these parameters as well as the details of one mixing event. We also found a limiting case in which the canonical value of the mixing efficiency 0.2 is recovered. The time-averaged Thorpe scale and the Ozmidov scale are derived from the turbulent kinetic energy equation following Dillon (1982) and Garrett (2001), and are compared with past microstructure measurements.

A mixing event that results from shear instability mixes via two distinct mechanisms that occur in sequence (e.g., Smyth et al. 2001, 2007). The first is preturbulent mixing, in which a growing, wavelike disturbance exerts a persistent, compressive strain on the scalar gradients, sharpening the gradients and thereby

accelerating the diapycnal scalar flux. This mixing occurs with relatively little dissipation of the kinetic energy and is in this sense highly efficient. The second mechanism is turbulence, which develops as the instability grows beyond some amplitude threshold. In contrast to preturbulent mixing, turbulence exerts a strain field that varies rapidly in time. As a result, scalar gradients do not have time to adjust to the optimal orientation for compression (Smyth 1999). This rapidly fluctuating turbulent strain is also effective at dissipating kinetic energy, with the net result that instantaneous mixing efficiency is reduced to somewhere near the canonical value 0.2. Our central conclusion here is that, in a forced mixing event, forcing governs mixing efficiency by altering the relative duration and intensity of the preturbulent and turbulent phases.

Detailed results may be summarized as follows:

- When Re_0 and b are fixed, Γ_c varies weakly as a function of Ri_{\min} and ω/N . In this parameter space, the relation between the growth rate of KH billows and the arrival of the deceleration phase controls mixing. When Ri_{\min} and ω/N are high, there is no mixing because the deceleration phase suppresses mixing. If Ri_{\min} or ω/N is sufficiently reduced, KH billows can grow, pair, and break even though deceleration suppresses the latter part of the mixing event. Because highly efficient preturbulent mixing (Smyth et al. 2001) dominates the time-averaged diapycnal flux and less efficient turbulence after breakdown is suppressed by the deceleration, Γ_c has relatively high values (around 0.3).
- Higher Re_0 and larger b act to accelerate the initial growth and secondary instability of the KH billows (e.g., Smyth et al. 2007). KH billows can grow before the deceleration phase arrives, thus changing the intensity of the mixing as well as Γ_c . When both Re_0 and b are higher and ω/N is smaller, the effects of deceleration become less important. However, if the forcing does not accelerate the mean flow long enough, Γ_c in higher Re_0 runs is larger than 0.3 because of efficient mixing late in the preturbulent phase.
- When Ri_{\min} and ω/N become small, KH billows onset before Ri_{\min} is achieved. Then, the intense but less efficient turbulence acts over a long time before deceleration begins and therefore contributes more to the net mixing than the highly efficient preturbulent mixing; thus, Γ_c is near the canonical value of 0.2, even in the case with higher Re_0 .
- Following the length-scale arguments of Dillon (1982) and Garrett (2001), the turbulent kinetic energy equation can be written in terms of three nondimensional numbers; Γ_c , R_{OT} (the ratio of the Ozmidov

scale L_O to the Thorpe scale L_T), and R_{BT} (the ratio of the buoyancy scale L_B to the Thorpe scale) and averaged over one event. Both L_O versus L_T and Γ_c versus R_{OT} diagrams can capture the transition from suppression to acceleration of the turbulent phase by the forcing. Those relationships are consistent with the observations in cases where turbulence is able to develop and persist before mean flow deceleration. Further tests of this scaling with in situ microstructure observations may allow us to study the dependence of mixing efficiency on forcing in high Reynolds number turbulence, which we cannot explore using present-day computers, and to verify our central conclusion in the ocean where forcing fields are more complicated.

Our study cannot investigate all of the relevant parameter ranges because of the limitations of current computer resources. Effects of high Reynolds number and multiple pairing of billows should be examined further. Effects of subsequent forcing need to be studied in high-frequency cases. An improved model of progressive interfacial waves (e.g., Woods 1968) could be attained by altering the phase relationship between the tilt angle and the mean flow such that $\bar{u}(z) = 0$ when $|\tau|$ is a maximum. Although our modeling is suitable for exploring the relations between time-varying forcing and Γ , the present configuration does not capture the broad range of internal wave breaking in the ocean where the effects of vertical propagation, convective instability, earth rotation, and the spatial variability of the shear field should be included (e.g., Lelong and Dunkerton 1998a,b). Reproducing internal wave breaking via wave-wave interaction (e.g., McEwan 1973) in DNS would also give more information about Γ within context of the ocean mixing.

Acknowledgments. This work is supported by the Office of Naval Research, the Natural Sciences and Engineering Research Council of Canada, and the National Science Foundation (Grants OCE0095640 and OCE0622922). Computation has been performed on the Western Canada Research Grid (WestGrid). We gratefully acknowledge Chris Garrett for useful discussions and Jeff Carpenter at the University of British Columbia for his help with the computations. Our manuscript was greatly improved by the comments made by two anonymous reviewers.

APPENDIX

Errors in Energy Diagnostics

The energy diagnostics and the three-dimensional density reordering computation used in this study are

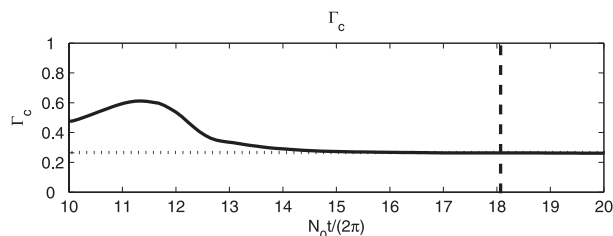


FIG. A1. Time series of Γ_c ($Ri_{\min} = 0.08$ and $\omega/N = 0.05$). Horizontal axis is dimensionless in time. Thick dotted line is Γ_c from the potential energy difference between $\omega t = \pi$ and $\omega t = 2\pi$. Thick dashed line is time when $Mn_i = 1$ is achieved.

only strictly correct when the tilting angle is 0. Thus, we assess the errors in the diagnostics by comparing Γ_c from the density reordering method with the cumulative mixing efficiency Γ_c from the differences in the potential energies at $\omega t = \pi$ and $\omega t = 2\pi$ (end of one forcing cycle). We use run AD7 (Fig. 2) for comparison; thus, we can also assess the effects of termination before one forcing cycle is completed. The time series of Γ_c at each time step [$t_2 = t$ in (28)] and Γ_c from the potential energy difference show that there is almost no difference at $\omega t = 2\pi$ ($t_{nd} = 20$ in Fig. A1): Γ_c is 0.262 and that from the potential energy difference is 0.265 (about 1% difference). We note that there is also almost no difference between Γ_c at $t_{nd} = 18.05$ ($Mn_i = 1$ is achieved at the end of the mixing; $\Gamma_c = 0.263$) and Γ_c at $\omega t = 2\pi$ (less than 1% difference). The same analysis with other DNS runs suggests that the errors in the diagnostics are within a few percent and our results are robust.

REFERENCES

- Arneborg, L., 2002: Mixing efficiencies in patchy turbulence. *J. Phys. Oceanogr.*, **32**, 1496–1506.
- Bouruet-Aubertot, P., and S. A. Thorpe, 1999: Numerical experiments on internal gravity waves in an accelerating shear flow. *Dyn. Atmos. Oceans*, **29**, 41–63.
- , C. R. Koudella, C. Staquet, and K. B. Winters, 2001: Particle dispersion and mixing by breaking internal gravity waves. *Dyn. Atmos. Oceans*, **33**, 95–134.
- Carpenter, J. C., G. A. Lawrence, and W. D. Smyth, 2007: Evolution and mixing of asymmetric Holmboe instabilities. *J. Fluid Mech.*, **582**, 103–132.
- Caulfield, C., and W. Peltier, 2000: Anatomy of the mixing transition in homogeneous and stratified free shear layers. *J. Fluid Mech.*, **413**, 1–47.
- Crawford, W. A., 1986: A comparison of length scales and decay times of turbulence in stably stratified flows. *J. Phys. Oceanogr.*, **16**, 1847–1854.
- Dillon, T. M., 1982: Vertical overturns: A comparison of Thorpe and Ozmidov length scales. *J. Geophys. Res.*, **87**, 9601–9613.
- Fringer, O. B., and R. L. Street, 2003: The dynamics of breaking progressive interfacial waves. *J. Fluid Mech.*, **494**, 319–353.

- Galbraith, P. S., and D. E. Kelley, 1996: Identifying overturns in CTD profiles. *J. Atmos. Oceanic Technol.*, **13**, 688–702.
- Gargett, A. E., and J. N. Moum, 1995: Mixing efficiencies in turbulent tidal fronts: Results from direct and indirect measurements of the density flux. *J. Geophys. Res.*, **81**, 1180–1196.
- Garrett, C., 2001: Stirring and mixing: What are the rate controlling processes? *From Stirring to Mixing in a Stratified Ocean: Proc. 'Aha Huliko' a Winter Workshop*, Honolulu, HI, University of Hawaii at Manoa, 1–8.
- , and L. St. Laurent, 2002: Aspects of deep ocean mixing. *J. Oceanogr.*, **58**, 11–24.
- Gregg, M. C., 1987: Diapycnal mixing in the thermocline: A review. *J. Geophys. Res.*, **92**, 5249–5286.
- , 1989: Scaling turbulent dissipation in the thermocline. *J. Geophys. Res.*, **94**, 9686–9698.
- Hazel, P., 1972: Numerical studies of the stability of inviscid stratified shear flows. *J. Fluid Mech.*, **51**, 39–61.
- Holmboe, J., 1962: On the behaviour of symmetric waves in stratified shear layers. *Geophys. Publ.*, **24**, 67–113.
- Howard, L. N., 1961: Note on a paper of John W. Miles. *J. Fluid Mech.*, **10**, 509–512.
- Imberger, J., and G. N. Ivey, 1991: On the nature of turbulence in a stratified fluid. Part II: Application to lakes. *J. Phys. Oceanogr.*, **21**, 659–680.
- Ivey, G. N., and J. Imberger, 1991: On the nature of turbulence in a stratified fluid. Part I: The energetics of mixing. *J. Phys. Oceanogr.*, **21**, 650–658.
- Klaassen, G., and W. Peltier, 1985: The onset of turbulence in finite-amplitude Kelvin–Helmholtz billows. *J. Fluid Mech.*, **155**, 1–35.
- , and —, 1989: The role of transverse secondary instabilities in the evolution of free shear layers. *J. Fluid Mech.*, **202**, 367–402.
- , and —, 1991: The influence of stratification on secondary instability in free shear layers. *J. Fluid Mech.*, **227**, 71–106.
- Koop, C. G., 1976: Instability and turbulence in a stratified shear layer. NSF–ONR Rep., Dept. of Aerospace Engineering, University of Southern California, Los Angeles, CA, 134 pp.
- Kundu, P. K., and I. M. Cohen, 2008: *Fluid Mechanics*. 4th ed. Academic Press, 872 pp.
- Lelong, M. P., and T. J. Dunkerton, 1998a: Inertia–gravity wave breaking in three dimensions. Part I: Convectively stable waves. *J. Atmos. Sci.*, **55**, 2473–2488.
- , and —, 1998b: Inertia–gravity wave breaking in three dimensions. Part II: Convectively unstable waves. *J. Atmos. Sci.*, **55**, 2489–2501.
- Linden, P. F., 1979: Mixing in stratified fluids. *Geophys. Astrophys. Fluid Dyn.*, **13**, 3–23.
- McEwan, A. D., 1973: Interactions between internal gravity waves and their traumatic effect on a continuous stratification. *Bound.-Layer Meteorol.*, **5**, 159–175.
- Miles, J. W., 1961: On the stability of heterogeneous shear flows. *J. Fluid Mech.*, **10**, 496–508.
- , and L. N. Howard, 1964: Note on a heterogeneous shear flow. *J. Fluid Mech.*, **20**, 331–336.
- Moum, J. N., 1996: Efficiency of mixing in the main thermocline. *J. Geophys. Res.*, **101**, 12 057–12 069.
- , D. M. Farmer, W. D. Smyth, L. Armi, and S. Vagle, 2003: Structure and generation of turbulence at interfaces strained by solitary waves propagating shoreward over the continental shelf. *J. Phys. Oceanogr.*, **33**, 2093–2112.
- Munk, W., 1981: Internal waves and small-scale processes. *Evolution of Physical Oceanography*, B. A. Warren and C. Wunsch, Eds., The MIT Press, 264–291.
- , and C. Wunsch, 1998: Abyssal recipes II: Energetics of tidal and wind mixing. *Deep-Sea Res. I*, **45**, 1977–2010.
- Oakey, N. S., 1982: Determination of the rate of dissipation of turbulent energy from simultaneous temperature and velocity shear microstructure measurements. *J. Phys. Oceanogr.*, **12**, 256–271.
- , 1985: Statistics of mixing parameters in the upper ocean during JASIN phase 2. *J. Phys. Oceanogr.*, **15**, 1662–1675.
- Osborn, T. R., 1980: Estimates of the local rate of vertical diffusion from dissipation measurements. *J. Phys. Oceanogr.*, **10**, 83–89.
- Ozmidov, R. V., 1965: On the turbulent exchange in a stably stratified ocean. *Izv. Acad. Sci. USSR Atmos. Oceanic Phys. Engl. Transl.*, **1**, 853–860.
- Peltier, W., and C. Caulfield, 2003: Mixing efficiency in stratified shear flows. *Annu. Rev. Fluid Mech.*, **35**, 136–167.
- Polzin, K. L., J. M. Toole, and R. W. Schmitt, 1995: Finescale parameterizations of turbulent dissipation. *J. Phys. Oceanogr.*, **25**, 306–328.
- , —, J. R. Ledwell, and R. W. Schmitt, 1997: Spatial variability of turbulent mixing in the abyssal ocean. *Science*, **276**, 93–96.
- Ruddick, B., D. Walsh, and N. Oakey, 1997: Variation in apparent mixing efficiency in the North Atlantic Central Water. *J. Phys. Oceanogr.*, **27**, 2589–2605.
- Seim, H., and M. Gregg, 1994: Detailed observations of a naturally occurring shear instability. *J. Geophys. Res.*, **99**, 10 049–10 073.
- , and —, 1995: Energetics of a naturally occurring shear instability. *J. Geophys. Res.*, **100**, 4943–4958.
- Simmons, H. L., R. W. Hallberg, and B. K. Arbic, 2004: Internal wave generation in a global baroclinic tidal model. *Deep-Sea Res. II*, **51**, 3043–3068.
- Smyth, W. D., 1999: Dissipation range geometry and scalar mixing in sheared, stratified turbulence. *J. Fluid Mech.*, **401**, 209–242.
- , and J. Moum, 2000: Length scales of turbulence in stably stratified mixing layers. *Phys. Fluids*, **12**, 1327–1342.
- , —, and D. Caldwell, 2001: The efficiency of mixing in turbulent patches: Inferences from direct simulations and microstructure observations. *J. Phys. Oceanogr.*, **31**, 1969–1992.
- , J. Nash, and J. Moum, 2005: Differential diffusion in breaking Kelvin–Helmholtz billows. *J. Phys. Oceanogr.*, **35**, 1004–1022.
- , J. C. Carpenter, and G. A. Lawrence, 2007: Mixing in symmetric Holmboe waves. *J. Phys. Oceanogr.*, **37**, 1566–1583.
- Staquet, C., 2000: Mixing in a stably stratified shear layer: Two- and three-dimensional numerical experiments. *Fluid Dyn. Res.*, **27**, 367–404.
- St. Laurent, L., and R. W. Schmitt, 1999: The contribution of salt fingers to vertical mixing in the North Atlantic Tracer Release Experiment. *J. Phys. Oceanogr.*, **29**, 1404–1424.
- Sun, H., and E. Kunze, 1999: Internal wave–wave interactions. Part II: Spectral energy transfer and turbulence production. *J. Phys. Oceanogr.*, **29**, 2905–2919.
- Thompson, R. O. R. Y., 1980: Efficiency of conversion of kinetic energy to potential energy by a breaking internal gravity wave. *J. Geophys. Res.*, **85**, 6631–6635.
- Thorpe, S. A., 1968: A method of producing a shear flow in a stratified fluid. *J. Fluid Mech.*, **32**, 693–704.

- , 1971: Experiments on the instability of stratified shear flows: Miscible fluids. *J. Fluid Mech.*, **46**, 299–319.
- , 1973: Turbulence in stably stratified fluid: A review of laboratory experiments. *Bound.-Layer Meteor.*, **5**, 95–119.
- , 1977: Turbulence and mixing in a Scottish loch. *Philos. Trans. Roy. Soc. London*, **286A**, 125–181.
- Wijesekera, H. W., and T. M. Dillon, 1997: Shannon entropy as an indicator of age for turbulent overturns in the oceanic thermocline. *J. Geophys. Res.*, **102**, 3279–3292.
- Winters, K. B., and E. A. D’Asaro, 1996: Diapycnal flux and the rate of fluid mixing. *J. Fluid Mech.*, **317**, 179–193.
- , P. N. Lombard, J. J. Riley, and E. A. D’Asaro, 1995: Available potential energy and mixing in density-stratified flows. *J. Fluid Mech.*, **289**, 115–128.
- Woods, J., 1968: Wave-induced shear instability in the summer thermocline. *J. Fluid Mech.*, **32**, 791–800.
- Wunsch, C., and R. Ferrari, 2004: Vertical mixing, energy, and the general circulation of the oceans. *Annu. Rev. Fluid Mech.*, **36**, 281–314.